Chemical Science

ROYAL SOCIETY OF CHEMISTRY

EDGE ARTICLE

View Article Online
View Journal

Cite this: DOI: 10.1039/d6sc01140c

All publication charges for this article have been paid for by the Royal Society of Chemistry

Interlayer co-chemistry of a homologous ion stabilizer and microenvironmental molecular regulator for high-performance zinc-ion storage

Keyi Chen,[a] Quan Zong, *[a] Yuqing Ji,[a] Helixin Jiao,[a] Qiaoling Kang,[a] Qilong Zhang,[b] Shuang Zhou,[d] Qianqian Wang,[e] Guoying Wei,[a] Zhihao Lou[a] and Anqiang Pan *[cd]

Received 9th February 2026
Accepted 6th March 2026

DOI: 10.1039/d6sc01140c

rsc.li/chemical-science

Layered materials have been regarded as ideal electrodes for aqueous zinc-ion batteries (ZIBs) due to their flexible 2D structures. However, their electrochemical properties remain limited by sluggish Zn^{2+} transport and structural instability caused by unsatisfactory interlayer chemistry including small interlayer distances, strong electrostatic interactions and structure collapse. Herein, we propose an interlayer co-chemistry strategy that integrates homologous Zn^{2+} stabilizers with a dipolar molecular regulator, triethylene glycol (TEG), to construct a compatible and dynamic interlayer environment in hydrate vanadium pentoxide. Combined theoretical and experimental evidence confirms that pre-intercalated Zn^{2+} anchors the VO layers to stabilize the layered structure and forms predefined transport channels through the homologous ion effect, while TEG regulates the local electric field, lowers Zn^{2+} desolvation barriers, and promotes rapid diffusion. In addition, the oxygen-containing groups of TEG further provide reversible Zn-binding sites, contributing additional storage capacity. As a result, the (TEG, Zn)–VOH cathode delivers a high specific capacity of 460 mAh g^{-1} at 0.1 A g^{-1}, excellent rate performance (301 mAh g^{-1} at 5 A g^{-1}), and outstanding cycling stability (106% capacity retention after 10 000 cycles at 8 A g^{-1}).

Introduction

Aqueous zinc ion batteries (ZIBs) have gained widespread attention as promising alternatives for next-generation large-scale energy-storage technologies, benefiting from their intrinsic safety, cost-effectiveness, and environmental friendliness compared with conventional lithium-ion batteries.[1–4] Despite these merits, the practical application of ZIBs remains constrained by the intrinsic limitations of current cathode materials, such as sluggish reaction kinetics, an unstable structure during cycling and insufficient active sites.[5–8] These issues lead to inadequate discharge capacity, poor rate capability, and unsatisfactory cycle life, thereby failing to meet the requirements of high-energy, long-life aqueous batteries.[9,10] Therefore, developing high-performance cathode materials with fast ion transport, robust structural stability, and optimized electrochemical reaction pathways is essential for advancing practical ZIBs.

Among various cathode materials, vanadium-based oxides have attracted considerable attention due to their rich redox activity and open framework capable of accommodating multivalent ions.[11–13] Nevertheless, vanadium-based oxides still suffer from sluggish Zn^{2+} diffusion originating from strong electrostatic interactions, severe structural collapse during repeated ion insertion/extraction, and side reactions associated with active water, leading to rapid capacity decay and unsatisfactory rate performance.[14–16] To address these challenges, previous studies have focused on guest-species pre-intercalation, either metal ions or organic cations/molecules, to adjust the interlayer spacing or suppress structural degradation.[17–19] Monovalent ions such as Na^+, K^+, and NH_4^+, and divalent ions such as Mg^{2+} or Ca^{2+} could enhance the initial structural robustness; however, they introduce ionic lattice distortion caused by radius/charge mismatch and competition with Zn^{2+} during cycling that increase Zn^{2+} migration barriers and impede fast ion diffusion.[20,21] Compared with hetero-cation pre-intercalation, homologous Zn^{2+} pillars could possibly provide a matched charge density and coordination environment, create pre-defined diffusion channels and eliminate ion-competition effects in subsequent cycling.[22] Therefore, homologous Zn^{2+} pre-intercalation provides a structurally rational and

[a]College of Materials and Chemistry, China Jiliang University, Hangzhou 310018, Zhejiang, People's Republic of China. E-mail: quanzong@cjlu.edu.cn
[b]State Key Lab of Silicon and Advanced Semiconductor Materials, Zhejiang University, Hangzhou 310027, Zhejiang, People's Republic of China
[c]School of Materials Science and Engineering, Xinjiang University, Urumqi 830017, Xinjiang, People's Republic of China
[d]School of Materials Science & Engineering, Central South University, Changsha 410083, Hunan, People's Republic of China. E-mail: pananqiang@csu.edu.cn
[e]School of Science, Huzhou University, Huzhou 313001, Zhejiang, People's Republic of China

electrochemically favorable strategy for achieving durable and fast zinc-ion storage.

Organic species have also been incorporated into layered vanadium oxides to enlarge interlayer spacing, extend the operating voltage window, and regulate the electrode/electrolyte interface.[23–25] Owing to their intrinsic structural diversity and functional groups, these organic components can improve the electronic conductivity of the host lattice and introduce additional redox-active or adsorption sites.[26,27] More recently, the role of organic intercalants has evolved from simple spacers to microenvironment regulators that create electrostatically favorable, Zn^{2+}-compatible interlayers capable of directing ion migration pathways.[28] However, compared to metal ion pre-intercalation, their weak coordination with the VO_x lattice fails to provide sufficient structural reinforcement, leading to framework collapse, molecular leaching, and ultimately limited cycling stability.[29,30] Therefore, rationally designing an interlayer co-chemistry that integrates the complementary benefits of inorganic and organic intercalants has become a key strategy to bridge the gap between stability and capacity.

In this work, we propose the interlayer co-chemistry engineering strategy *via* introducing homologous zinc ions and flexible triethylene glycol (TEG) molecules to regulate the lattice microenvironment (Fig. 1). Homologous Zn^{2+} functions as an ionic stabilizer, developing strong interaction with the framework and forming predefined transport channels to effectively suppress irreversible structural collapse during repeated cycling. The TEG molecule with dipole has the ability to regulate the local electric field within the interlayer region, reducing Zn^{2+} desolvation barriers, weakening electrostatic interaction, and promoting rapid Zn^{2+} diffusion. Additionally, the oxygen-containing groups of TEG offer extra Zn-storage sites through reversible weak coordination, contributing a molecular-level storage mechanism beyond redox chemistry. Comprehensive experimental characterization studies combined with theoretical calculations elucidate the role of Zn^{2+} and TEG in modifying the crystal structure, electronic structure and interlayer electrochemical behavior of the hybrid cathode. As a result, the cathode exhibits outstanding electrochemical performance, delivering high capacities of 460 mAh g^{-1} and 301 mAh g^{-1} at 0.1 A g^{-1} and 5 A g^{-1}, as well as stable cycling performance (106% capacity retention after 10 000 cycles at 10 A g^{-1}).

Results and discussion

The crystal structures of the prepared VOH, Zn–VOH, TEG–VOH, and (TEG, Zn)–VOH samples were first characterized by X-ray diffraction (XRD), as shown in Fig. 2a. The diffraction peaks of pristine VOH are well indexed with the $V_2O_5 \cdot 1.6H_2O$ phase (JCPDS no. 40-1296), where lattice water molecules are located in the bilayered vanadium oxide framework.[31] The characteristic (001) diffraction peak is located at approximately 7.6°, corresponding to an interlayer spacing of 11.6 Å. Upon the intercalation of either Zn^{2+} ions or TEG molecules into the VOH host structure, the (001) diffraction peak exhibits a shift toward lower angles, indicating an expansion of the lattice spacing to 13.2 Å and 13.9 Å, respectively. The incorporation of TEG not only induces larger interlayer spacing, possibly ascribed to its larger molecular volume compared with Zn^{2+} ions, but also leads to a significant attenuation of the (001) peak intensity originating from the changed growth direction. Notably, when Zn^{2+} and TEG are co-intercalated, the (001) diffraction peak appears between the positions observed for the Zn–VOH and TEG–VOH samples, indicating that the interlayer spacing falls between the two samples. This intermediate value suggests a synergistic intercalation effect, wherein Zn^{2+} provides electrostatic anchoring to stabilize the layered host while TEG introduces steric spacing, yielding a balanced and structurally

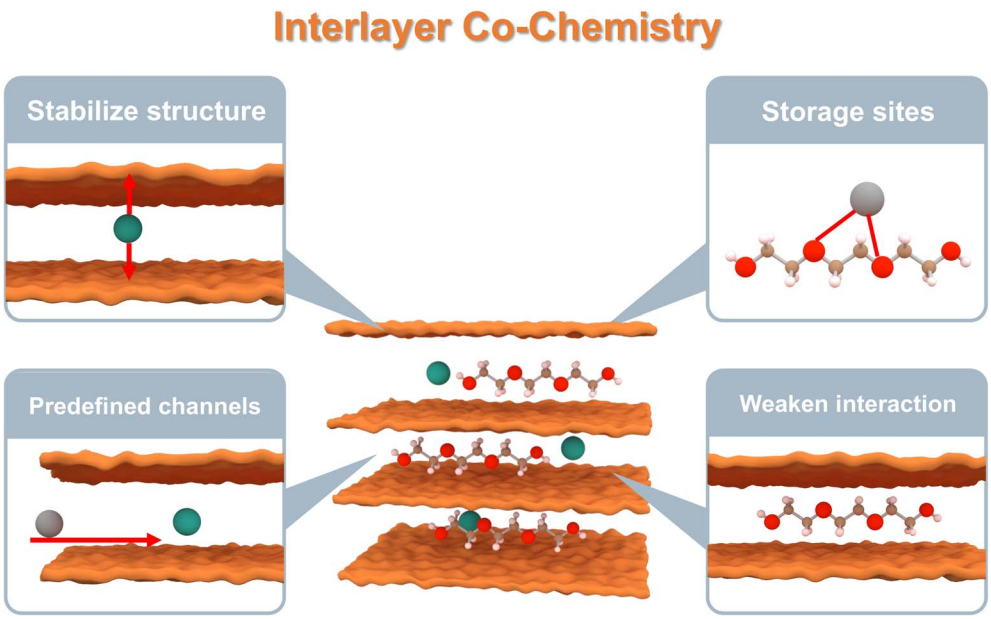

Fig. 1 Illustration of the interlayer co-chemistry.

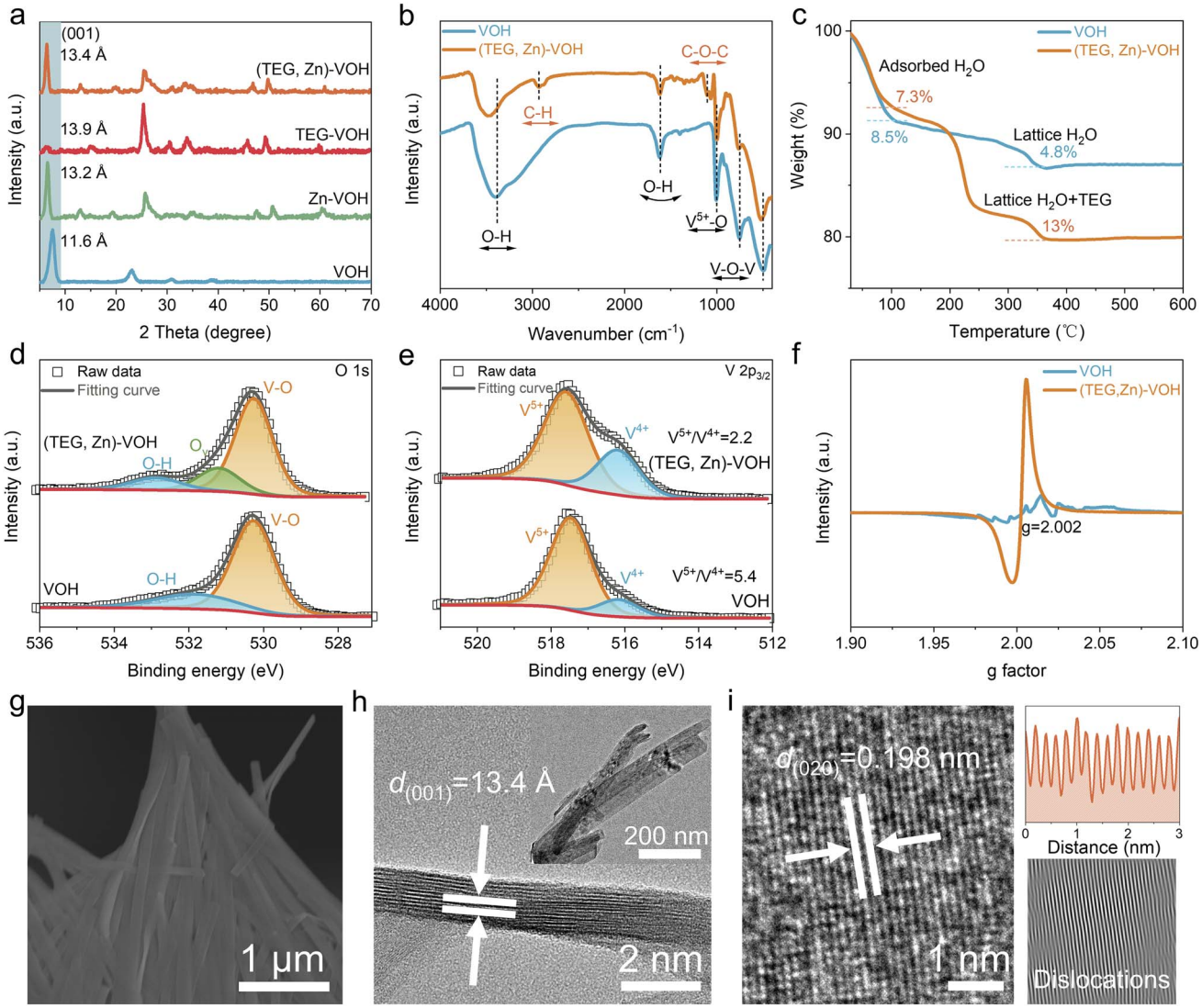

Fig. 2 Structure and chemical environment of VOH and (TEG, Zn)–VOH. (a) XRD patterns. (b) FTIR spectra. (c) TG curves. High-resolution XPS spectra of (d) O 1s and (e) V $2p_{3/2}$. (f) EPR spectra. (g) SEM image of (TEG, Zn)–VOH. (h) TEM images of (TEG, Zn)–VOH. (i) HRTEM image and corresponding IFFT pattern of (TEG, Zn)–VOH.

moderated expansion relative to either species alone. Fourier-transform infrared (FT-IR) spectroscopy was employed to identify the functional groups present in VOH and (TEG, Zn)–VOH materials (Fig. 2b). The spectrum of (TEG, Zn)–VOH displays characteristic absorption bands at approximately 1100 cm^{-1} and 2900 cm^{-1}, which are assigned to the C–O–C stretching vibration and C–H stretching vibration of TEG molecules, respectively.[32,33] These characteristic peaks are absent in the spectrum of pristine VOH, providing direct evidence for the successful intercalation of TEG. Compared with VOH, (TEG, Zn)–VOH shows a blue shift in the peaks of V–O–V and O–H stretching vibrations, which is attributed to the strong interaction between TEG/Zn^{2+} and the VOH framework. The decreased peak intensity in (TEG, Zn)–VOH may result from the disruption of partial V–O bonds and the formation of oxygen defects with the introduction of TEG and Zn^{2+}. Thermogravimetric analysis (TGA) curves (Fig. 2c) reveal that the mass loss observed below 100 °C is attributed to the removal of physically adsorbed water, with weight losses of 8.5% for VOH and 7.3% for (TEG, Zn)–VOH. The mass loss in the temperature range of 100–350 °C primarily originates from the elimination of lattice water and the decomposition of TEG molecules. It is noteworthy that the total mass loss of (TEG, Zn)–VOH in this stage reaches 10.7%, higher than the 4.8% observed for VOH. Combined with inductively coupled plasma-optical emission spectroscopy (ICP-OES, Table S1), the chemical formulae of VOH and (TEG, Zn)–VOH are determined to be $V_2O_5 \cdot 0.56H_2O$ and $TEG_{0.18}Zn_{0.27}V_2O_{4.96} \cdot 0.37H_2O$, respectively.

As illustrated in Fig. 2d, the O 1s XPS spectrum of pristine VOH can be deconvoluted into two characteristic peaks assigned to lattice oxygen (V–O) and coordinated water molecules. In contrast, the spectrum of (TEG, Zn)–VOH exhibits a new peak component ascribed to oxygen vacancies (O_v). The high-resolution V $2p_{3/2}$ XPS spectra reveal the presence of mixed

valence states of V^{5+} and V^{4+} in both VOH and (TEG, Zn)–VOH.[34] The V^{5+}/V^{4+} ratio decreases from 5.4 for VOH to 2.2 for (TEG, Zn)–VOH, indicating the reduction of V^{5+} during the co-intercalation process. This phenomenon is commonly associated with the formation of oxygen vacancies, which is beneficial for enhancing electronic conductivity and increasing active sites for ion storage. Electron paramagnetic resonance (EPR) spectra further provide direct evidence that this co-intercalation process effectively induces the formation of oxygen vacancies (Fig. 2f).[35] (TEG, Zn)–VOH exhibits a strong symmetric signal at $g = 2.002$, which is the characteristic response of unpaired electrons associated with oxygen vacancies. In contrast, the pristine VOH shows only a very weak signal. Scanning electron microscopy (SEM) images (Fig. S1) reveal the nanosheet morphology of VOH and TEG–VOH. When incorporated with Zn^{2+}, the nanobelt clusters self-assemble into a three-dimensional interconnected network, which is homogeneously grown on the carbon cloth substrate (Fig. 2g and S2). Compared to the two-dimensional membrane structure of pristine VOH, this 3D morphology induced by the co-intercalation of ions and molecules may offer an increased contact area for electrolyte penetration and ion transport. Energy dispersive spectroscopy (EDS) elemental mappings (Fig. S3) reveal that the elements of C, V, O and Zn are also homogeneously distributed within the whole (TEG, Zn)–VOH sample, providing further evidence of successful TEG and Zn^{2+} insertion into the VOH framework. High-resolution transmission electron microscopy (HRTEM) characterization (Fig. 2h) shows the ultrathin nanobelt structure of (TEG, Zn)–VOH. The measured (001) interplanar spacing is 13.4 Å, which is highly consistent with the XRD analysis results. The corresponding selected area electron diffraction (SAED) pattern (Fig. S4) displays the nanocrystalline structure. Furthermore, a lattice spacing of 0.198 nm is observed in Fig. 2i, corresponding to the (020) crystal plane of (TEG, Zn)–VOH. The corresponding Inverse Fast Fourier Transform (IFFT) analysis displays various lattice dislocations, which are caused by oxygen vacancies.

Fig. 3a compares the third cyclic voltammetry (CV) profiles of all samples at a scan rate of 0.1 mV s^{-1} within a voltage window of 0.2–1.6 V. All samples exhibit two pairs of distinct redox peaks, corresponding to the redox reactions of V^{5+}/V^{4+} and V^{4+}/V^{3+}, respectively. Compared with VOH, the (TEG, Zn)–VOH sample shows an enhanced peak intensity, indicating an improved charge storage capability and accelerated electrochemical reaction kinetics. In comparison with other electrodes, the (TEG, Zn)–VOH electrode has a smaller voltage gap between the anodic and cathodic peaks (Fig. S5), indicating suppressed polarization. In addition, the discharge peaks shift to higher voltages in subsequent cycles, possibly due to changes in the local chemical environment following Zn^{2+} insertion. Fig. 3b displays the galvanostatic charge–discharge (GCD) curves of each electrode at a current density of 0.1 A g^{-1}. The curves show two voltage plateaus at ~1.0 V and ~0.6 V, which are consistent with the positions of the redox peaks in the CV curves, indicating the two-step ion storage mechanism. The (TEG, Zn)–VOH electrode delivers a discharge capacity of 460 mAh g^{-1}, which is higher than that of VOH (260 mAh g^{-1}), Zn–VOH (355 mAh g^{-1}), and TEG–VOH (399 mAh g^{-1}). In addition, the overlapped CV and GCD curves in the first three cycles (Fig. S6 and S7) mean a reversible reaction of the (TEG, Zn)–VOH cathode in the aqueous Zn-ion battery. The rate capabilities of the four electrodes at various current densities from 0.5 A g^{-1} to 5 A g^{-1} are shown in Fig. 3c. The average discharge capacities of (TEG, Zn)–VOH at current densities of 0.5, 1, 2, 4, and 5 A g^{-1} are the highest among all electrodes, which are 417, 388, 359, 320, and 301 mAh g^{-1}, respectively. When the current density is restored to 0.1 A g^{-1}, its capacity can recover to 390 mAh g^{-1}, confirming excellent kinetic reversibility. The corresponding voltage profiles at various current densities (Fig. S8) indicate that (TEG, Zn)–VOH exhibits a distinct charging voltage plateau and reduced voltage polarization. In addition, (TEG, Zn)–VOH displays an average capacity of 196 mAh g^{-1} at −20 °C and 0.5 A g^{-1}, indicating good tolerance to low temperature (Fig. S9). The enhanced capacity and high reversibility originate from the increased active sites and strong Zn^{2+} capture ability of TEG molecules.

Fig. 3d compares the long-term cycling stability of all electrodes at a low current density of 0.5 A g^{-1}. After 200 cycles, the (TEG, Zn)–VOH electrode maintains a high capacity retention rate of 92%, which outperforms VOH (54%), Zn–VOH (73%), and TEG–VOH (61%). The (TEG, Zn)–VOH cathode also exhibited excellent cycling stability and reversibility at high current densities (4.0 A g^{-1} and 8.0 A g^{-1}) (Fig. S10 and 2e). At 8 A g^{-1}, the VOH electrode exhibits a disappointing capacity retention rate of only 33% after 10 000 cycles. The Zn–VOH electrode has an initial discharge capacity of 79 mAh g^{-1}, which increases to 95 mAh g^{-1} after 10 000 cycles, indicating that Zn^{2+} can stabilize the overall structure. Although TEG–VOH delivers a high initial capacity of 120 mAh g^{-1}, its retention drops to 63% after 10 000 cycles. This capacity fading may be attributed to the large ion size of TEG and its weak interaction with the $[VO_n]$ layers. In contrast, (TEG, Zn)–VOH exhibits an enhanced initial capacity of 204 mAh g^{-1} and maintains 106% capacity retention after 10 000 cycles, underscoring the synergistic effect of dual TEG/Zn^{2+} intercalation in stabilizing the layered framework and facilitating reversible Zn^{2+} storage. The slight increase in capacity in the initial several cycles could be attributed to the activation process or electrolyte penetration. Additionally, the SEM image of (TEG, Zn)–VOH after 10 000 cycles (Fig. S11) shows that its structure still maintains the interconnected morphology, which proves its excellent structural stability. Self-discharge behavior was examined in full cells to evaluate the reliability of the TEG/Zn^{2+} co-intercalation strategy (Fig. S12). After resting for 48 h at the fully charged state, the Zn‖(TEG, Zn)–VOH cell maintained an open-circuit voltage (OCV) of 1.46 V and a high capacity retention of 85.3%, superior to the Zn‖VOH cell (1.25 V, 81.1%). Moreover, the electrolyte containing the (TEG, Zn)–VOH electrode shows no noticeable color change compared to that with the VOH electrode after immersion, indicating effectively suppressed vanadium dissolution (Fig. S13). These results confirm that the (TEG, Zn)–VOH cathode effectively suppresses side reactions and stabilizes the electrode/electrolyte interface.

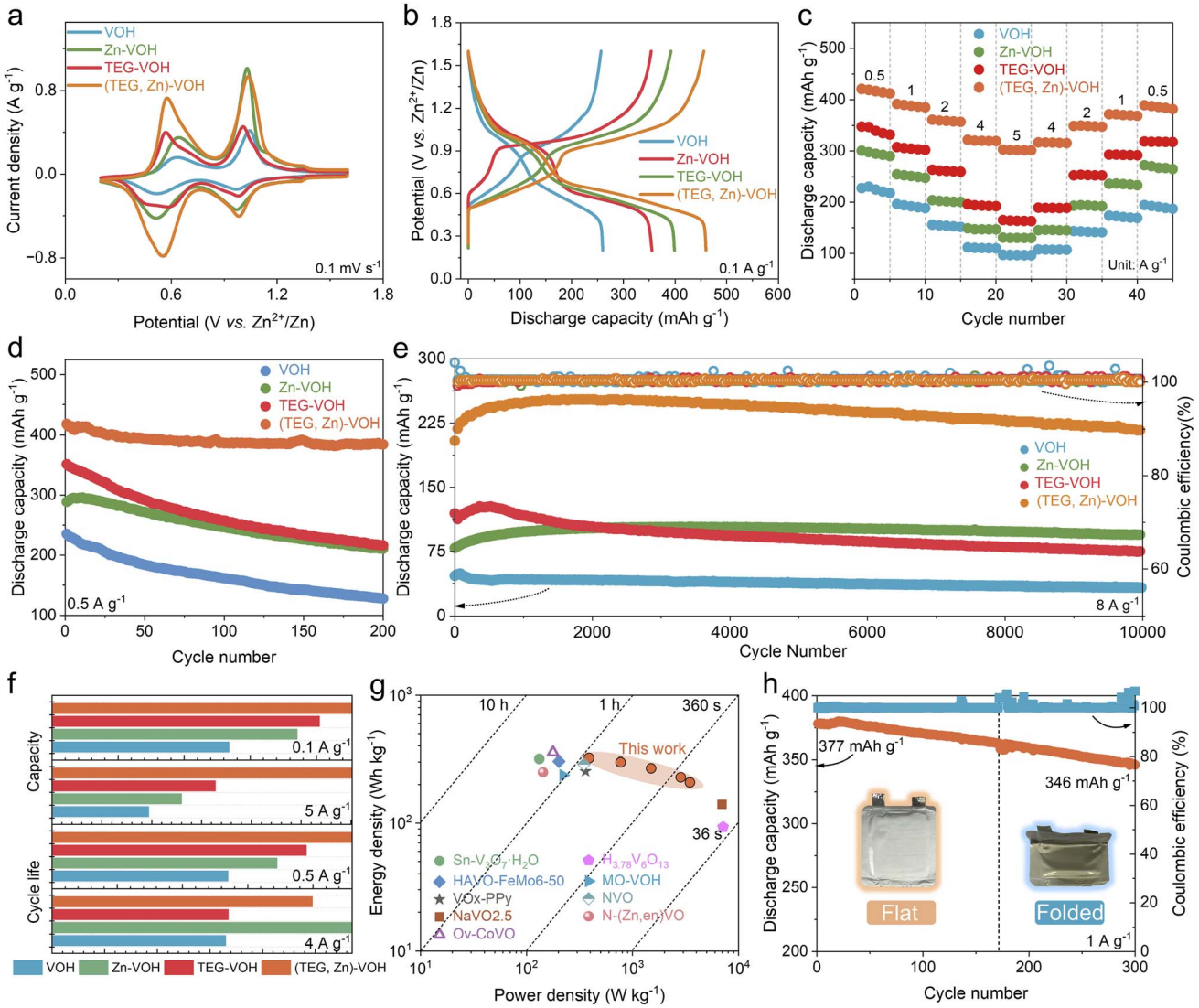

Fig. 3 Electrochemical properties of all electrodes. (a) CV curves at 0.1 mV s^{-1}. (b) Voltage profiles at 0.1 A g^{-1}. (c) Rate performance. Cycle stability at (d) 0.5 A g^{-1} and (e) 8 A g^{-1}. (f) Comparison of capacity and cycle life of all samples. (g) Ragone plots. (h) Cycling performance of Zn||(TEG, Zn)–VOH pouch cells at flat and folded states.

Fig. 3f provides a comprehensive comparison of the structural and electrochemical properties of all electrodes. The homologous Zn^{2+} pillars within the interlayers effectively reinforce the host structure, mitigating lattice collapse during repeated ion insertion and extraction. The TEG molecule with inherent high conductivity and functional groups accelerates ion/electron mobility and provides storage sites, contributing to the high capacity and rate capability. Consequently, the (TEG, Zn)–VOH electrode demonstrates a well-balanced integration of high reversible capacity, outstanding rate capability, and exceptional cycling durability, outperforming many previously reported cathode materials (Table S1). The (TEG, Zn)–VOH electrode also delivers a high energy density of 322 Wh kg^{-1} at a power density of 388 W kg^{-1} and retains 208 Wh kg^{-1} at a high power output of 3477 W kg^{-1}. As shown in Fig. 3g, the energy-power characteristics of (TEG, Zn)–VOH surpass those of most recently reported vanadium-based oxide cathodes.[36–44] To further assess its practical applicability, a flexible pouch cell was assembled using metallic Zn as the anode, (TEG, Zn)–VOH as the cathode, and a $Zn(OTf)_2$ electrolyte. As shown in Fig. 3h, the pouch cell exhibits a good capacity retention rate at a current density of 1 A g^{-1}, and no significant capacity degradation is observed when the battery is bent. This result demonstrates that the obtained pouch battery has excellent flexibility and feasibility.

Fig. 4a and S14 display the CV curves of (TEG, Zn)–VOH and VOH at scan rates ranging from 0.2 to 1.2 mV s^{-1}. With increasing scan rate, the cathodic peaks gradually shift toward higher potentials, while the anodic peaks move to lower potentials, indicating the increased electrochemical polarization during Zn^{2+} insertion/extraction. To quantitatively analyze the charge-storage mechanisms, the *b*-values were obtained by fitting the relationship between peak current density and scan rate.[45,46] For the (TEG, Zn)–VOH electrode, the calculated *b*-

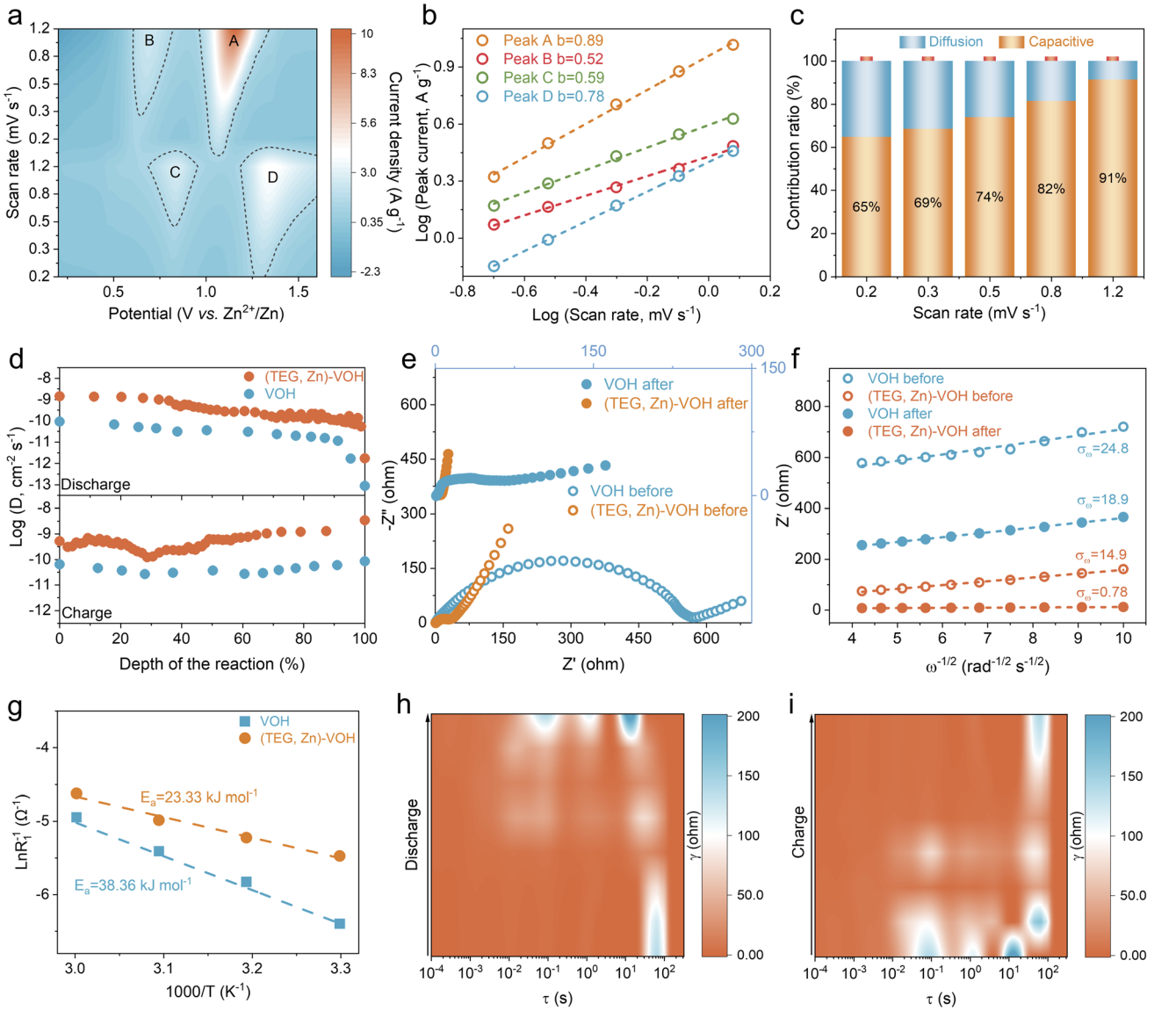

Fig. 4 Electrochemical kinetics of VOH and (TEG, Zn)–VOH. (a) CV contour plots of (TEG, Zn)–VOH. (b) Corresponding log(*i*) *vs.* log(*v*) plots. (c) Capacitive contributions of (TEG, Zn)–VOH at various scan rates. (d) $D_{Zn^{2+}}$ calculated from GITT curves. (e) EIS spectra before and after the CV test. (f) *Z′ vs.* $\omega^{-1/2}$ plots. (g) ln(1/R_{ct}) *vs.* 1000/*T* plots. *In situ* DRT curves during (h) discharge and (i) charge.

values for peaks A, B, C, and D are 0.89, 0.52, 0.59, and 0.78, respectively (Fig. 4b). These results indicate that the V^{5+}/V^{4+} redox process is largely dominated by surface-controlled capacitive behavior, whereas the V^{4+}/V^{3+} transition is mainly governed by the diffusion process. Moreover, the CV profile at 0.5 mV s^{-1} reveals a high capacitive contribution of 74% for (TEG, Zn)–VOH (Fig. S15).[47,48] As the scan rate increases from 0.2 to 1.2 mV s^{-1}, the capacitive contribution progressively increases from 65% to 91% (Fig. 4c), demonstrating an increasingly capacitive-dominated charge-storage mechanism at high rates, which contributes to the superior rate performance. In comparison with VOH, (TEG, Zn)–VOH exhibits higher *b*-values and surface-capacitive contributions (Fig. S16 and S17), highlighting the accelerated Zn^{2+} reaction kinetics enabled by the dual intercalation of TEG and Zn^{2+}.

The Zn^{2+} diffusion behavior in the bulk electrodes of VOH and (TEG, Zn)–VOH was quantitatively assessed using the galvanostatic intermittent titration technique (GITT) (Fig. S18). As shown in Fig. 4d, (TEG, Zn)–VOH exhibits Zn^{2+} diffusion coefficient ($D_{Zn^{2+}}$) values approximately in the range of 10^{-8} to 10^{-10} cm^2 s^{-1} during the charge/discharge process, which are higher than those of VOH ($\approx 10^{-10}$ to 10^{-13} cm^2 s^{-1}). This indicates improved ion diffusion kinetics, attributable to the expanded interlayer spacing and weak electrostatic interaction induced by Zn^{2+} and TEG incorporation. Electrochemical impedance spectroscopy (EIS) plots before and after the CV tests and the corresponding equivalent circuit are depicted in Fig. 4e and S19. Prior to the CV tests, the charge transfer resistance (R_{ct}) of (TEG, Zn)–VOH is about 40 Ω, significantly lower than the 567 Ω for VOH, indicating enhanced charge transfer kinetics. After the

CV tests, the R_{ct} values decrease for both electrodes, reaching 7 Ω for (TEG, Zn)–VOH and 58 Ω for VOH, primarily due to the electrochemical activation. The Zn^{2+} diffusion characteristics are further evaluated *via* the relationship between the real part of impedance (Z') and $\omega^{-1/2}$. The slope of this line corresponds to the Warburg factor (σ_ω), where a smaller value indicates faster ion diffusion.[49,50] As shown in Fig. 4f, the (TEG, Zn)–VOH electrode presents smaller σ_ω compared to VOH before and after CV, suggesting accelerated ion transport kinetics within the electrode. The desolvation behavior at the electrode/electrolyte interface was investigated *via* EIS plots at different temperatures.[51,52] The (TEG, Zn)–VOH electrode exhibits smaller R_{ct} than VOH in the temperature range of 30–60 °C (Fig. S20), indicating enhanced interfacial charge-transfer kinetics. Based on Arrhenius analysis derived from plots of $\ln(1/R_{ct})$ *versus* $1000/T$, the activation energy (E_a) is calculated to be 38.36 kJ mol^{-1} for VOH and reduced to 23.33 kJ mol^{-1} for (TEG, Zn)–VOH (Fig. 4g). The lower E_a for (TEG, Zn)–VOH suggests a facilitated Zn^{2+} desolvation process at the electrode/electrolyte interface, which can be attributed to the abundant –OH functionalities in TEG that regulate the interfacial solvation environment and lower the energy barrier for ion transfer. The *in situ* distribution of relaxation times (DRT) analysis originating from EIS plots during the charge/discharge process (Fig. S21) further reveals the time constant of the electrochemical process of the (TEG, Zn)–VOH electrode.[53–55] As shown in Fig. 4h, during the discharge process, the characteristic peaks continuously shift toward shorter relaxation times (τ), indicating an acceleration of charge transfer kinetics and Zn^{2+} diffusion as Zn^{2+} insertion proceeds. In contrast, the gradual reduction of the DRT intensity ($\gamma(\tau)$) means the acceleration of Zn^{2+} transport within the electrode following the continue extraction/desorption of Zn^{2+} during the charge process (Fig. 4i). The magnitude of the $\gamma(\tau)$ for (TEG, Zn)–VOH is lower than that of VOH across all frequency ranges, indicating the enhancements in both interfacial charge transfer and bulk ionic diffusion properties (Fig. S22). These results reveal that (TEG, Zn)–VOH exhibits faster Zn^{2+} transport, enhanced pseudocapacitive behavior, and superior electrochemical kinetics compared to VOH.

To elucidate the electrochemical reaction mechanism of the (TEG, Zn)–VOH cathode, comprehensive *ex situ* characterization studies were carried out to monitor structural evolution and chemical-state transitions at various charge–discharge stages. *Ex situ* XRD patterns at different electrochemical states in Fig. 5a show that a shift of the (001) diffraction peak toward higher angles with a decreased intensity is observed during the discharge process, indicating the contraction of the interlayer spacing and the reduced crystallinity due to Zn^{2+} intercalation. Upon charging, this peak partially recovers to its initial state, suggesting a reversible structural evolution. Moreover, the appearance and disappearance of the characteristic peaks belonging to the $Zn_3(OH)_2V_2O_7\cdot 2H_2O$ (ZVO) by-product further demonstrate a reversible formation–dissolution process that is attributed to the reversible Zn^{2+} and H^+ co-insertion/extraction behaviors.[56,57] Fig. 5b presents the *ex situ* FTIR spectra of the (TEG, Zn)–VOH electrode in the fully charged and discharged states. When discharged to 0.2 V, the intensity of characteristic peaks related to TEG is weakened, which may be attributed to the chelating effects between the Zn^{2+} and TEG. Upon charging to 1.6 V, the peak intensities are strengthened, indicating that TEG undergoes a reversible binding/release process and participates in the storage of Zn^{2+}. In the *ex situ* high-resolution XPS spectra of C 1s (Fig. 5c), the peak intensities of C–O–C and C–OH decrease during discharging and recover in the fully discharged state due to the reversible reaction between Zn^{2+} and TEG, indicating that TEG can act as energy storage sites. The *ex situ* V $2p_{3/2}$ spectra (Fig. 5d) reveal dynamic and reversible changes among V^{3+}, V^{4+}, and V^{5+} oxidation states. The reversible changes in their relative intensities during charge and discharge confirm the involvement of multi-valent vanadium redox reactions in the electrochemical reaction process. During the discharging process, the decreased peak of V–O in the O 1s spectra (Fig. 5e) suggests the reduced crystallinity and generated ZVO caused by the proton insertion. The persistent oxygen vacancy signal suggests that defect sites remain structurally stable throughout cycling. The Zn 2p spectra exhibit two peaks at 1046.0 eV (Zn $2p_{1/2}$) and 1022.9 eV (Zn $2p_{3/2}$) after discharging to 0.2 V, with an intensity reduction upon charging to 1.6 V (Fig. 5f), confirming the reversible insertion and extraction of Zn^{2+} ions.

The corresponding HRTEM images show that the interlayer distances of the fully discharged and charged (TEG, Zn)–VOH electrodes are 11.9 Å and 13.4 Å (Fig. 5g), respectively, coinciding well with the *ex situ* XRD results. In addition, the *ex situ* SEM images reveal the generation/decomposition of the ZVO microsheets on the fully discharged/charged electrode surface caused by the reversible proton intercalation/deintercalation (Fig. 5h). EDS elemental mappings (Fig. 5i) show homogeneous distributions of V, O, C, and Zn elements. The intensified Zn signal after discharge and its partial removal after charging provide further evidence for the reversible storage behavior of Zn^{2+}.

The molecular electrostatic potential (ESP) map of the TEG molecule is illustrated in Fig. 6a, in which regions with positive potential correspond to electrophilic sites, while regions with negative potential indicate nucleophilic domains.[58] The oxygen atoms exhibit high electronegativity, resulting in negative electrostatic potentials in these regions. Conversely, the hydrogen atoms bonded to these atoms display positive potentials. This distribution enables the TEG molecule to effectively attract and stabilize Zn^{2+} when interacting with them, thereby enhancing reaction kinetics and storage capacity. Fig. 5b and c display the density of states (DOS) calculation for VOH and (TEG, Zn)–VOH, respectively. Compared to VOH, (TEG, Zn)–VOH exhibits a significantly increased DOS near the Fermi level and the conduction band crosses the Fermi level, indicating enhanced metallic conductive behavior.[59] This modulation of the electronic structure, originating from orbital hybridization induced by the co-intercalated species, significantly improves the intrinsic electronic conductivity of the material. The comparison of the charge density difference for VOH and (TEG, Zn)–VOH is shown in Fig. 6d and S23. Zn^{2+} develops a strong chemical bond with O^{2-} in the framework, which ensures the structural stability. In addition, the charge

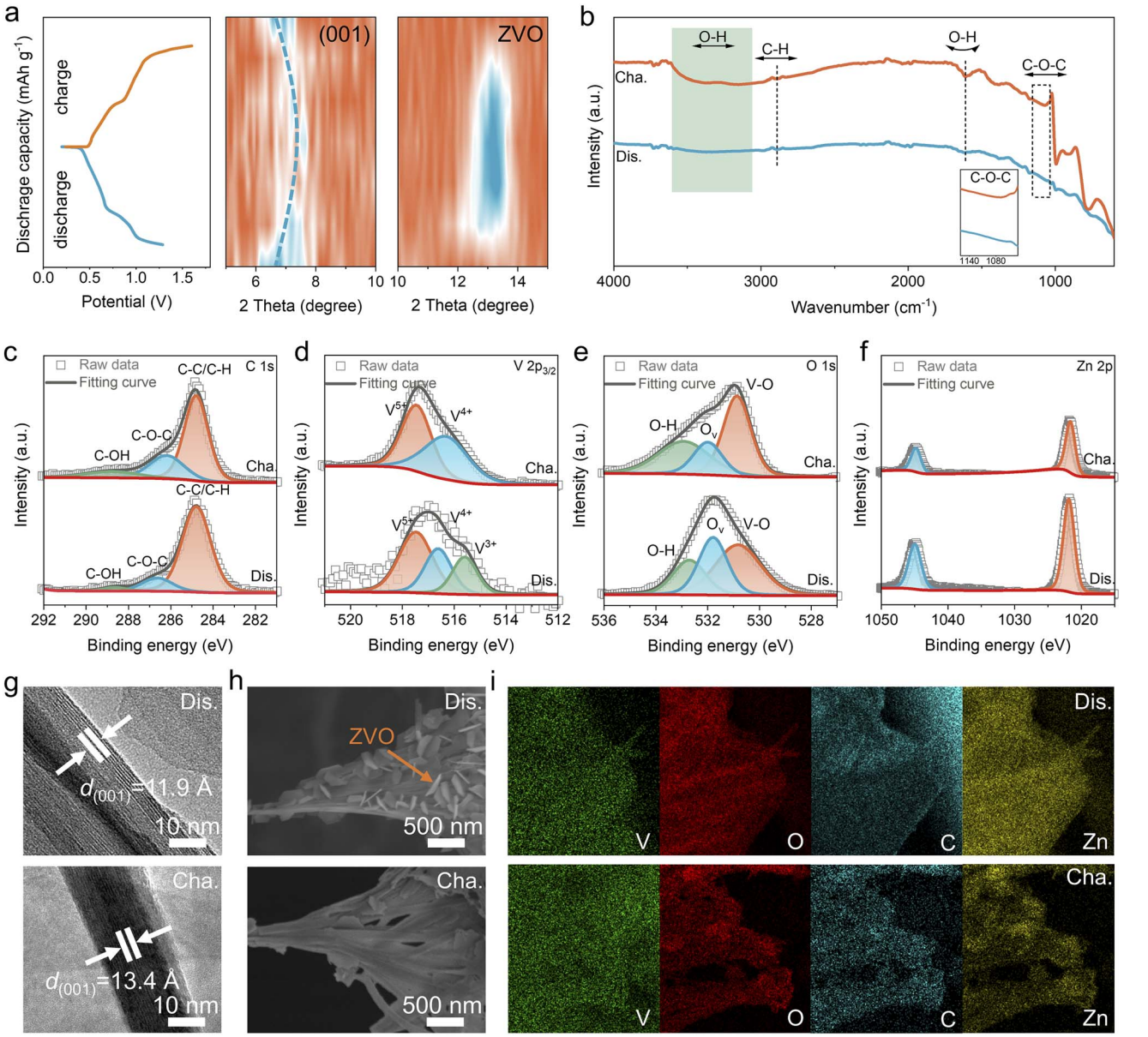

Fig. 5 Energy storage mechanism of (TEG, Zn)–VOH. (a) *Ex situ* XRD patterns. (b) *Ex situ* FTIR spectra. *Ex situ* XPS spectra of (c) C 1s, (d) V $2p_{3/2}$, (e) O 1s, and (f) Zn 2p. (g) *Ex situ* HRTEM images. (h) *Ex situ* SEM images. (i) *Ex situ* EDS mappings.

redistribution is clearly observed with the insertion of TEG molecules, resulting in the weaker electrostatic interaction between TEG and the [VO_n] layer, which is more conducive to the improvement of diffusion kinetics and electrochemical properties. The possible Zn^{2+} migration pathways within the VOH and (TEG, Zn)–VOH framework are shown in Fig. 6e and S24. As shown in Fig. 6f, the ion diffusion energy barrier calculated for (TEG, Zn)–VOH is 0.34 eV, which is lower than 0.91 eV in VOH. This indicates that the interplanar spacing is expanded by TEG and Zn^{2+}, and the electrostatic interactions between the VOH framework and Zn^{2+} are mitigated by TEG, thereby promoting ion diffusion within the VOH structure.

Fig. 6g summarizes the synergistic mechanism of TEG and Zn^{2+} co-intercalation. The pre-intercalated Zn^{2+} act as "pillars" to stabilize the layered structure and expand the ion diffusion channels, while the TEG molecules further reduce electrostatic reactions and act as extra energy storage sites to accelerate the reaction kinetics. Their synergistic work ultimately enables rapid and stable zinc-ion storage. The energy storage mechanism of (TEG, Zn)–VOH is schematically summarized in Fig. 6h. During the discharge process, hydrated Zn^{2+} undergo rapid desolvation and migrate into the layered framework, leading to a contraction of the interlayer spacing. The intercalated TEG molecules modulate the interlayer chemical environment and act as additional reversible storage sites, effectively lowering the Zn^{2+} migration barrier and accelerating solid-state diffusion, thereby enhancing both capacity and reaction kinetics. Upon charging, Zn^{2+} and H^+ are extracted from the host lattice, and

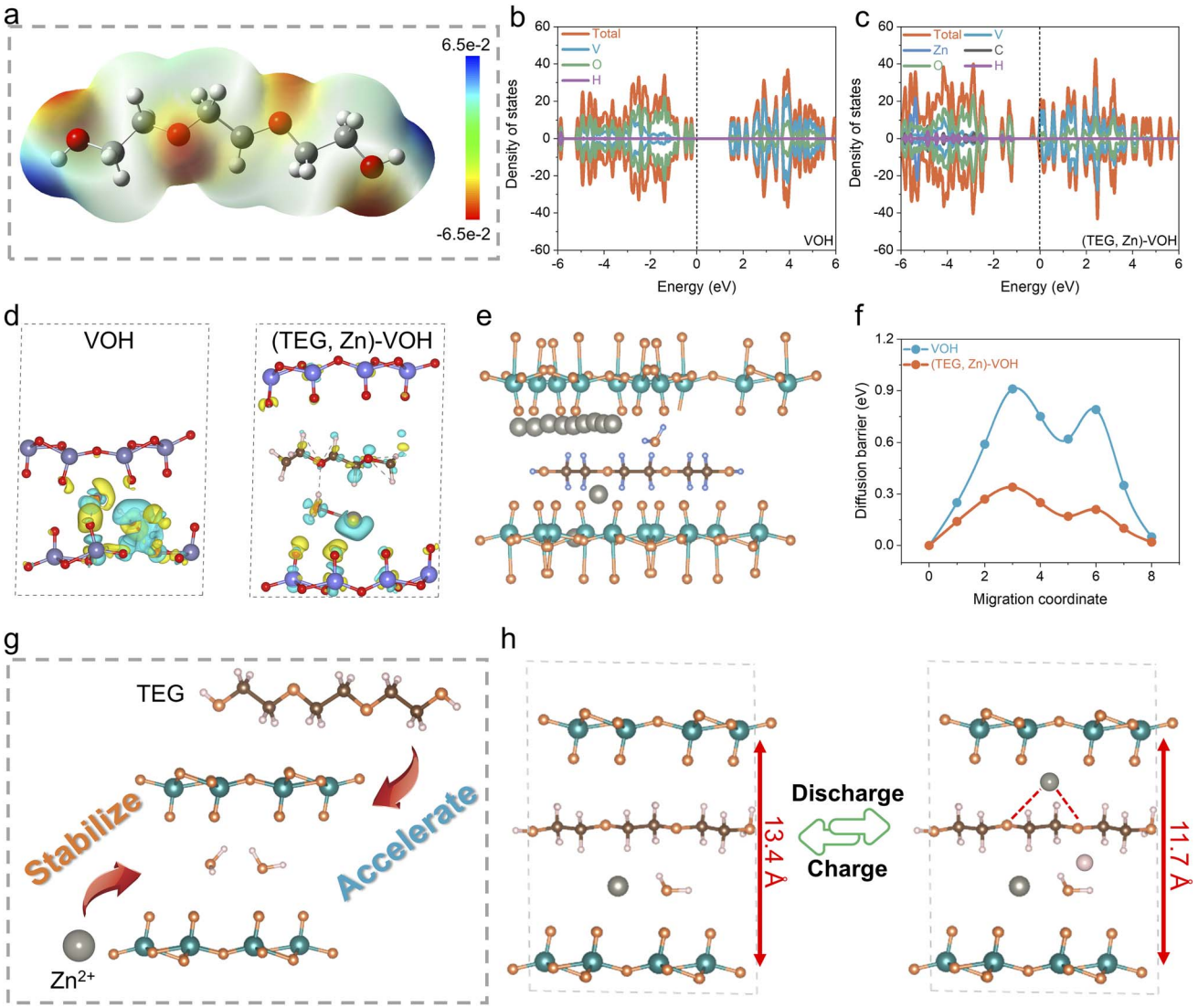

Fig. 6 Theoretical calculation results. (a) ESP mapping of the TEG molecule. DOS of (b) VOH and (c) (TEG, Zn)–VOH. (d) Charge density difference of VOH and (TEG, Zn)–VOH. (e) Possible Zn^{2+} migration pathway in (TEG, Zn)–VOH. (f) Diffusion barriers of Zn^{2+} for VOH and (TEG, Zn)–VOH. (g) Effects of Zn^{2+} and TEG on the VOH framework. (h) Schematic diagram of the Zn^{2+} storage mechanism in (TEG, Zn)–VOH.

the interlayer structure returns to its initial state, demonstrating a highly reversible structural evolution throughout the electrochemical cycle.

Conclusion

In summary, homologous zinc ions and flexible TEG molecules were introduced into the interlayers of VOH as a structural stabilizer and microenvironmental molecular regulator. The incorporation of Zn^{2+} appears to develop interaction with the adjacent vanadium-oxide layer, suppress structural dissolution and preserve lattice integrity, thus ensuring the stability of the whole structure. On the other hand, TEG molecules increase the interlayer spacing of the crystal structure, disrupt the solvation structure of hydrated Zn^{2+} and weaken the electrostatic interaction, thereby accelerating the desolvation and diffusion process of Zn^{2+}. Additionally, the polar groups provide supplementary active sites that act as electron donors to bind Zn^{2+}, forming a dual energy storage mechanism that enhances overall electrochemical performance. Both theoretical calculation and experimental tests demonstrate the promoting effect of Zn^{2+} and TEG, including decreased desolvation energy, a fast ion transfer/diffusion rate, and enhanced electronic conductivity. As a result, the (TEG, Zn)–VOH electrode exhibits superior electrochemical performance, including high capacity (460 mAh g^{-1} at 0.1 A g^{-1}), outstanding rate capability, and a long cycle life of 10 000 cycles at 8 A g^{-1}, surpassing most reported vanadium-based cathodes.

Author contributions

Keyi Chen: conceptualization, investigation, data curation, writing-original draft. Quan Zong: conceptualization, supervision, funding acquisition, writing-review & editing. Yuqing Ji:

investigation, data curation. Helixin Jiao: investigation. Qiaoling Kang: software, resources. Qilong Zhang: resources. Shuang Zhou: resources, methodology. Qianqian Wang: resources. Guoying Wei: resources, supervision. Zhihao Lou: supervision. Anqiang Pan: writing – review & editing, supervision.

Conflicts of interest

There are no conflicts to declare.

Data availability

The data supporting this article have been included as part of the supplementary information (SI). Supplementary information is available. See DOI: https://doi.org/10.1039/d6sc01140c.

Acknowledgements

This work was supported by the National Natural Science Foundation of China (Grant No. 52302322), the Zhejiang Provincial Natural Science Foundation of China (Grant No. LQ24E020004), the Fundamental Research Funds for the Provincial Universities of Zhejiang (2024YW13), and the Natural Science Foundation of Huzhou City (2021YZ06).

References

1 Y. Hu, P. Wang, M. Li, Z. Liu, S. Liang and G. Fang, *Energy Environ. Sci.*, 2024, **17**, 8078–8093.
2 D. Larcher and J. M. Tarascon, *Nat. Chem.*, 2015, **7**, 19–29.
3 Y. Liu, X. Lu, F. Lai, T. Liu, P. R. Shearing, I. P. Parkin, G. He and D. J. L. Brett, *Joule*, 2021, **5**, 2845–2903.
4 M. Tang, Q. Liu, X. Zou, B. Zhang and L. An, *Adv. Mater.*, 2025, **37**, 2501361.
5 A. Ali, J. Mohammadi Moradian, A. Naveed, S. Zhang, M. H. Tahir, K. Shehzad and M. Sillanpää, *Prog. Mater. Sci.*, 2026, **156**, 101543.
6 X. Chen, W. Li, D. Reed, X. Li and X. Liu, *Electrochem. Energy Rev.*, 2023, **6**, 33.
7 D. Gupta, S. Liu, R. Zhang and Z. Guo, *Adv. Energy Mater.*, 2025, **15**, 2500171.
8 K. Guo, Y. Lv, Z. Song, L. Gan and M. Liu, *Chem. Sci.*, 2026, **17**, 3936–3957.
9 G. Li, L. Sun, S. Zhang, C. Zhang, H. Jin, K. Davey, G. Liang, S. Liu, J. Mao and Z. Guo, *Adv. Funct. Mater.*, 2023, **34**, 2301291.
10 M. S. Javed, T. Najam, I. Hussain, M. Idrees, A. Ahmad, M. Imran, S. S. A. Shah, R. Luque and W. Han, *Adv. Energy Mater.*, 2022, **13**, 2202303.
11 K. Zhu and W. Yang, *Acc. Chem. Res.*, 2024, **57**, 2887–2900.
12 P. Hu, P. Hu, T. D. Vu, M. Li, S. Wang, Y. Ke, X. Zeng, L. Mai and Y. Long, *Chem. Rev.*, 2023, **123**, 4353–4415.
13 P. Liu, Z. Song, Q. Huang, Z. Xu, Y. Lv, L. Gan and M. Liu, *Angew. Chem., Int. Ed.*, 2026, e25690.
14 H. Liu, X. Hou, Q. Zhang, W. Peng, Y. Li and X. Fan, *Adv. Energy Mater.*, 2025, **15**, 2406171.
15 R. Sinha, X. Xie, Y. Yang, Y. Li, Y. Xue, P. Wang and Z. Li, *Adv. Energy Mater.*, 2025, **15**, 2404815.
16 T. Lv, Y. Peng, G. Zhang, S. Jiang, Z. Yang, S. Yang and H. Pang, *Adv. Sci.*, 2023, **10**, 2206907.
17 C. Liu, Z. Neale, J. Zheng, X. Jia, J. Huang, M. Yan, M. Tian, M. Wang, J. Yang and G. Cao, *Energy Environ. Sci.*, 2019, **12**, 2273–2285.
18 C. Zhang, X. Xu, Z. Chen, Q. Li, Y. Zhong, X. Wang, J. Tu and C. Gu, *Adv. Mater.*, 2025, **38**, e10792.
19 F. Wan, Z. Hao, S. Wang, Y. Ni, J. Zhu, Z. Tie, S. Bi, Z. Niu and J. Chen, *Adv. Mater.*, 2021, **33**, 2102701.
20 J. H. Liu, Y. Wang, X. Chen, Z. C. Jian, H. Jiang, H. Zhang, C. Wu, X. Jiang, Y. Gao, X. Cao and Y. Xiao, *Adv. Funct. Mater.*, 2025, **36**, e17823.
21 Y. Liu, J. Xu, J. Li, Z. Yang, C. Huang, H. Yu, L. Zhang and J. Shu, *Coord. Chem. Rev.*, 2022, **460**, 214477.
22 C. Fang, B. Xu, J. Han, X. Liu, Y. Gao and J. Huang, *Adv. Funct. Mater.*, 2024, **34**, 2310909.
23 X. Ma, X. Cao, M. Yao, L. Shan, X. Shi, G. Fang, A. Pan, B. Lu, J. Zhou and S. Liang, *Adv. Mater.*, 2022, **34**, 2105452.
24 H. Liu, H. Niu, W.-H. Huang, T. Shen, C. Li, C.-C. Chang, M. Yang, C. Gao, L. Yang, Q. Zong, Y. Pei, G. Cao and C. Liu, *ACS Energy Lett.*, 2024, **9**, 5492–5501.
25 L. Hu, Z. Wu, C. Lu, F. Ye, Q. Liu and Z. Sun, *Energy Environ. Sci.*, 2021, **14**, 4095–4106.
26 X. Lu, L. Chen, W. Li, X. Zhang, W. Chi, M. Peng, C. Wang, Y. Liu and X. Zhang, *Adv. Funct. Mater.*, 2025, **36**, e13457.
27 K. Guo, Z. Song, Y. Lv, L. Gan and M. Liu, *Adv. Funct. Mater.*, 2025, **35**, 2506036.
28 Y. Zhang, S. Gao, Q. Li, Y. Sun, L. Jiang, Y. Su, S. Cao, H. Yue and H. Pang, *Adv. Funct. Mater.*, 2025, e22432.
29 P. Zhang, Y. Gong, S. Fan, Z. Luo, J. Hu, C. Peng, Q. Zhang, Y. Li and X. Ren, *Adv. Energy Mater.*, 2024, **14**, 2401493.
30 F. Zhang, X. Sun, M. Du, X. Zhang, W. Dong, Y. Sang, J. Wang, Y. Li, H. Liu and S. Wang, *Energy Environ. Mater.*, 2020, **4**, 620–630.
31 Z. Chen, H. Liu, S. Fan, Q. Zhang, C. Yuan, W. Peng, Y. Li and X. Fan, *Adv. Energy Mater.*, 2024, **14**, 2400977.
32 W. He, Z. Lin, K. Zhao, Y. Li, C. Meng, J. Li, S. Lee, Y. Wu and X. Hao, *Adv. Mater.*, 2022, **34**, 2203920.
33 L. Peng, Y. Zhu, X. Peng, Z. Fang, W. Chu, Y. Wang, Y. Xie, Y. Li, J. J. Cha and G. Yu, *Nano Lett.*, 2017, **17**, 6273–6279.
34 J. Huang, H. Liang, Y. Tang, B. Lu, J. Zhou and S. Liang, *Adv. Energy Mater.*, 2022, **12**, 2201434.
35 X. Hu, S. Gao, T. Lin, X. Peng, Y. Huang, Y. Zhang, X. Yang, L. Wang, G. Luo, Z. Wen, B. Johannessen, S. Wang, L. Wang and B. Luo, *Adv. Mater.*, 2025, **37**, 2416714.
36 D. Zhang, J. Cao, C. Yang, K. Lolupiman, W. Limphirat, X. Wu, X. Zhang, J. Qin and Y. Huang, *Adv. Energy Mater.*, 2024, **15**, 2404026.
37 Y. Zhang, Q. Li, W. Feng, H. Yue, S. Gao, Y. Su, Y. Tang, J. Wu, Z. Zhang, Y. Zhang, M. Shakouri, H. C. Chen and H. Pang, *Angew. Chem., Int. Ed.*, 2025, **64**, e202501728.
38 D. Guo, Y. Fan, Q. Yang, M. Song, F. Zhang, J. Liu, Z. Zhu and H. Zhang, *Chem. Eng. J.*, 2025, **507**, 160745.
39 Y. D. Ma, H. N. Zhu, Y. Le, Y. H. Liu, T. H. Mei, S. J. Bao and M. W. Xu, *Rare Met.*, 2024, **44**, 230–239.

40 Z. Wang, P. Cui, X. Wang, M. Chang, Y. Yu, J. You, F. Hu, Y. Wu and K. Zhu, *Adv. Funct. Mater.*, 2024, **34**, 2407925.
41 J. Cao, D. Zhang, Y. Yue, X. Yang, C. Yang, J. Niu, Z. Zeng, P. Kidkhunthod, S. Wannapaiboon, X. Zhang, J. Qin and J. Lu, *Adv. Funct. Mater.*, 2023, **33**, 2307270.
42 R. Cui, J. Gu, N. Wang, Y. Wang, X. Huang, S. Zhang, L. Lu and D. Wang, *Small*, 2024, **20**, 2307849.
43 Y. Xu, G. Fan, P. X. Sun, Y. Guo, Y. Wang, X. Gu, L. Wu and L. Yu, *Angew. Chem., Int. Ed.*, 2023, **62**, e202303529.
44 F. Zhang, M. Du, Z. Miao, H. Li, W. Dong, Y. Sang, H. Jiang, W. Li, H. Liu and S. Wang, *InfoMat*, 2022, **4**, 12346.
45 M. Liu, X. Li, M. Cui, F. Chen, J. Li, W. Shi, Y. Liu, X. Li, Y. Wang, W. Zhang, C. Shao and Y. Liu, *Nat. Commun.*, 2024, **15**, 10769.
46 M. Yang, J. Zhu, J. Lin, L. He, M. Chen, Y. Wang, J. Chen, S. Zhong, H. Mi, C. He, D. Ma and P. Zhang, *Angew. Chem., Int. Ed.*, 2025, **64**, e202510893.
47 X. Xu, T. Wang, X. Zhao, X. Qu, L. Jiao and Y. Liu, *ACS Energy Lett.*, 2025, **10**, 5057–5066.
48 P. Yi, Z. Li, L. Ma, B. Feng, Z. Liu, Y. Liu, W. Lu, S. Cao, H. Fang, M. Ye and J. Shen, *Adv. Mater.*, 2024, **36**, 2414379.
49 H. Guo, M. Sotoudeh, S. Rezeki, Y. Hu, R. Leiter, J. Wellmann, M. Fichtner, M. Oschatz, A. Gross and S. Fleischmann, *Angew. Chem., Int. Ed.*, 2025, **138**, e20990.
50 Y. Zhu, R. Zhao, Y. Xu, W. Chen, Z. Hu, L. Xi, Y. Xie, H. Hou, T. Liu, K. Amine, X. Ji and G. Zou, *Adv. Mater.*, 2025, **37**, 2419582.
51 L. Ding, L. Wang, J. Gao, T. Yan, H. Li, J. Mao, F. Song, S. Fedotov, L. Y. Chang, N. Li, Y. Su, T. Liu and L. Zhang, *Adv. Funct. Mater.*, 2023, **33**, 2301648.
52 Z. Lv, R. Tang, C. Sun, W. Meng, J. Yang, S. Li, Q. Wu, M. Zhang, J. Zhao and Y. Yang, *Energy Environ. Sci.*, 2025, **18**, 762–773.
53 H. Hong, J. Zhu, Y. Wang, Z. Wei, X. Guo, S. Yang, R. Zhang, H. Cui, Q. Li, D. Zhang and C. Zhi, *Adv. Mater.*, 2024, **36**, 2308210.
54 M. Yang, Y. Wang, D. Ma, J. Zhu, H. Mi, Z. Zhang, B. Wu, L. Zeng, M. Chen, J. Chen and P. Zhang, *Angew. Chem., Int. Ed.*, 2023, **62**, e202304400.
55 X. Ding, Q. Zhu, Y. Fan, Y. Yang, L. Liu, Y. Shao, Y. Xiao, C.-H. Wu and L. Han, *Nano Energy*, 2025, **136**, 110701.
56 M. Wu, C. Shi, J. Yang, Y. Zong, Y. Chen, Z. Ren, Y. Zhao, Z. Li, W. Zhang, L. Wang, X. Huang, W. Wen, X. Li, X. Ning, X. Ren and D. Zhu, *Adv. Mater.*, 2024, **36**, 2310434.
57 V. Verma, S. Kumar, W. Manalastas and M. Srinivasan, *ACS Energy Lett.*, 2021, **6**, 1773–1785.
58 Y. Xia, Z. Hong, L. Zhou, S. Chen, Z. Luo, S. Jin, Y. Huang, Y. Jiang and Y. Wu, *J. Energy Chem.*, 2023, **87**, 153–161.
59 J. Ma, C. Li, Q. Ji, C. Liu, B. Tang, R. Liu, Y. Liu, N. Li, C. Wang, J. Zeng, K. Zheng and W. Yan, *Angew. Chem., Int. Ed.*, 2025, **64**, e202513148.